Misalignment Tolerance of Electric Vehicle Wireless Charging System Based on Reconfigurable Adaptive Topology and Centrosymmetric Coils

Zhongjin Huang, Chao Liu, Wenxuan Pan, Xiaoying Chen, Xingkui Mao, *Member, IEEE*, and Yiming Zhang, *Senior Member, IEEE*

***Abstract*—In wireless power transfer systems for electric vehicles, coil misalignment is inevitable in most charging situations. Most present studies concentrate on the misalignment tolerance in one direction, either in the *X*, *Y*, *Z*, or diagonal directions, but lack the misalignment tolerance on the whole charging plane. In this article, a reconfigurable adaptive topology and centrosymmetric coils are proposed to achieve misalignment tolerance over the whole charging plane. By switching among three operation modes of the proposed reconfigurable topology at the different misaligned regions, the output voltage at the boundary regions can be increased and the output voltage fluctuation can be limited. First, the mathematical model of the proposed reconfigurable adaptive topology in the different operation modes is investigated. Second, the design process of the magnetic coupler and the characteristics of the centrosymmetric coils are presented. Finally, a 926-W prototype is built to verify the proposed system. The experimental results demonstrate that the fluctuation of the output voltage is less than 21.3% apart from the four most corner regions, and the peak efficiency is 84.5%.**

***Index Terms*—Centrosymmetric coils, electric vehicles (EVs), misalignment tolerance, reconfigurable topology, wireless power transfer (WPT).**

I. Introduction

TO ADAPT to the development of green concepts in the new era, electric vehicles (EVs) are becoming more and more popular in the market. The development of EVs has also been accompanied by technological innovation [1], [2], [3]. The onboard charger (OBC) [4], [5], [6] and wireless power transfer (WPT) are two prime charging methods for EVs. OBC takes advantage of high efficiency and mature production segments but lacks convenience and safety. Wired charging cables can also take up much space and can be unaesthetic. Unlike OBC, WPT combines convenience, safety, and automation as advantages which has attracted more and more attention from academia and industry in recent years [7]. It can also be combined with OBC [8]. Application of WPT runs through various fields such as industry, autonomous underwater vehicle, and medical fields [9], [10], [11], [12].

The conventional WPT technology can be divided into inductive power transfer (IPT) and capacitive power transfer (CPT). CPT relies on the alternating electric field of two pairs of metal plates for power transfer. CPT is simple and inexpensive to manufacture, but it is inefficient and sensitive to surroundings [13]. In comparison, energy is transferred through the magnetic field of coupled coils for IPT, which is more efficient and has a longer charging distance. IPT is the most widely used method in WPT technologies [14].

The IPT system [15] usually consists of power converters, magnetic couplers, and resonant networks. The magnetic couplers are made up of the transmitting (Tx) and receiving (Rx) coils. In wireless charging for EVs, due to manual parking, the Tx and Rx coils often fail to align, resulting in positional deviations. This causes fluctuations in the mutual inductance of the transmitting and receiving coils, leading to fluctuations in the output voltage and a significant reduction in the efficiency of the charging system. Consequently, misalignment tolerance is one of the key research fields in EV wireless charging systems. The misalignments in a WPT system are usually referred to as *X* misalignment, *Y* misalignment, and diagonal misalignment, which are shown in Fig. 1. The transmitting coil is on the ground side, whereas the receiving coil is on the car side. *X* misalignment usually refers to the misalignment in the direction of the car going forward or backward. *Y* misalignment is also called door-to-door misalignment. To improve misalignment tolerance and the stability of the IPT systems, the modification of the magnetic coupler and the topology structure are investigated.

Typical magnetic couplers include the unipolar coil (Q), the bipolar coil (DD), the double-D quadruple coil (DDQ) [16], and the solenoid coil. In [17], the DD coil was used as the Tx and Rx coils to tolerate the misalignment and get a stable output power fluctuation in the *Y*-direction. However, the *X* misalignment tolerance was weak. A third-coil coupler was utilized to improve the misalignment tolerance in *X*- and *Y*-directions, but also did

Manuscript received 16 September 2023; revised 8 November 2023; accepted 15 December 2023. Date of publication 21 December 2023; date of current version 16 February 2024. This work was supported in part by the National Natural Science Foundation of China under Grant 52107183 and in part by the Natural Science Foundation of Fujian Province under Grant 2022J06011. Recommended for publication by Associate Editor K. Park. *(Corresponding authors: Yiming Zhang; Xiaoying Chen.)*

The authors are with the School of Electrical Engineering and Automation, Fuzhou University, Fuzhou 350108, China (e-mail: 220120026@fzu.edu.cn; 220110002@fzu.edu.cn; 220120033@fzu.edu.cn; fzucxy@fzu.edu.cn; mxk782@fzu.edu.cn; zym@fzu.edu.cn).

Color versions of one or more figures in this article are available at https://doi.org/10.1109/TPEL.2023.3345536.

Digital Object Identifier 10.1109/TPEL.2023.3345536

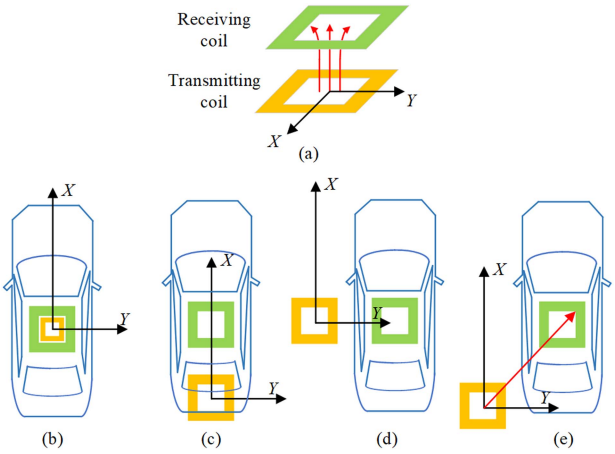

Fig. 1. Graphs of misalignment of receiving coil of three types. (a) and (b) Align well. (c) *X* misalignment. (d) *Y* misalignment. (e) Diagonal misalignment.

not affect the inherent output characteristics [18]. In [19], the quadruple-D quadrature pads were proposed to tolerate the *X*, *Y*, *Z*, and diagonal misalignments. However, the coil size was too large and the percentage of the misalignment was less than 50%. In [20], the integrated decoupling coils of two unipolar coils were introduced, which was efficient under the *X* or *Y* misalignment direction. However, the whole planar misalignment tolerance was not considered. In [21], the Rx coil was integrated into the compensation coil and the coil space was fully utilized. The *X*, *Y*, *Z*, and diagonal misalignment tolerance was achieved. However, the misalignment range study still does not cover the entire charging plane. In [22], one diode was replaced with an active switch. By controlling its state, the system could operate in a full-bridge rectifier mode or a half-bridge rectifier mode. The output power fluctuation of the proposed system was less than 17.5% along *X* or *Y* misalignments. However, the maximum output power was low. In [23], a clamp circuit and a reconfigurable rectifier were combined to improve coupling variation tolerance. The output power fluctuation was only 5% as the experiment showed. However, the maximum output power was only 400 W.

Four types of compensation topologies, namely series (S), parallel (P), inductor-capacitor-capacitor (*LCC*), and inductor-capacitor-inductor (*LCL*) can be combined on both the Tx and Rx sides. A dual-transmitter EV charging system with a reconfigurable topology was proposed to tolerate door-to-door misalignment in [24]. However, the degree of misalignment freedom needs improvement. In [25], an S-P topology was applied to the three-Rx system, which can be of high efficiency. However, the cost was high in designing the magnetic coupler and the output fluctuation was large. The hybrid topology of the input-parallel output-series connection can ensure the mutual inductance is stable within a certain elliptic region, but it decreases rapidly in the boundary regions [26]. S and *LCC* topologies were connected in parallel on the Rx side to implement misalignment tolerance in [27]; however, the misalignment tolerance just be reflected on *Y* misalignment. In [28], a relay coil was combined with the hybrid topology. A load-independent constant-current output and improved misalignment tolerance can be achieved with a relatively small number of compensation components. However, it only achieved the misalignment tolerance on the axis.

Through the above analysis, it can be concluded that the existing studies mainly concentrate on tolerating the *X*, *Y*, *Z*, and diagonal misalignments, but neglect the misalignment on the whole plane. To improve the misalignment tolerance over the whole plane, this article proposes a reconfigurable topology and centrosymmetric coils. Based on the topology, the system can switch among three working modes in different regions and utilize several dominant coil combinations to transfer energy in each region. The output voltage fluctuation can be limited and the output voltage on the boundary regions can be increased.

The rest of this article is organized as follows. Section II presents the operating modes of the proposed topology. The mathematical model is also analyzed. The design process of the magnetic coupler is clarified in Section III. The experimental results are presented in Section IV. Finally, Section V concludes this article.

II. Proposed Topology and Mathematical Model

A. Proposed Topology

The *LCC*-S topology is selected to tolerate weak couplings, as shown in Fig. 2(a). The unipolar coil is chosen as the Tx coil, and the proposed centrosymmetric coils and the cross-shaped coil are selected as the Rx coils, as shown in Fig. 2(b). L_1 is the Tx coil. L_{S1}–L_{S4} are the centrosymmetric Rx coils on the first layer. The coils of the same color belong to the same coil. L_{S5} is the cross-shaped Rx coil in the second layer. S_1–S_4 are four power MOSFETs of the inverter, and D_1–D_{12} are the rectifier diodes. U_I denotes the ac input voltage. V_{INV} and V_{REC} denote the dc voltages of the inverter and rectifier, respectively. U_{O1}, U_{O2}, U_{O3}, U_{O4}, and U_{O5} denote the ac output voltage of five branches, respectively. V_{REC1}, V_{REC2}, V_{REC3}, V_{REC4}, and V_{REC5} denote the dc output voltage of the five branches, respectively. M_1, M_2, M_3, M_4, and M_5 are the mutual inductances of the corresponding coils. L_F, C_F, and C_1 are the Tx compensation inductance and capacitors. C_{S1}, C_{S2}, C_{S3}, C_{S4}, and C_{S5} are the Rx compensation capacitors. R_L is the load resistance. I_F, I_1, I_{S1}, I_{S2}, I_{S3}, I_{S4}, and I_{S5} denote the rms values of the corresponding currents.

S_K, D_{K1}, and D_{K2} are the switches for mode transition between the series and parallel connection of the diode rectifier on the dc side. When S_K is OFF, D_{K1} and D_{K2} are both ON to provide two current paths for both layers of coils, and the dc output of the four parallel branches (L_{S1}–L_{S4}) are connected in parallel with the dc output of the cross-shaped coil L_{S5}. When S_K is ON, D_{K1} and D_{K2} are both OFF due to the reverse voltage, and the dc output of four parallel branches (L_{S1}–L_{S4}) are connected in series with the dc output of the cross-shaped coil L_{S5}, which ensures that the current paths of both layers of coils are the same.

For the use of rectifiers, the ac output of the four small coils is connected with four half-bridge rectifiers, whereas the ac output of the cross-shaped coil is connected with a full-bridge rectifier. The reason for different arrangements of rectifiers is

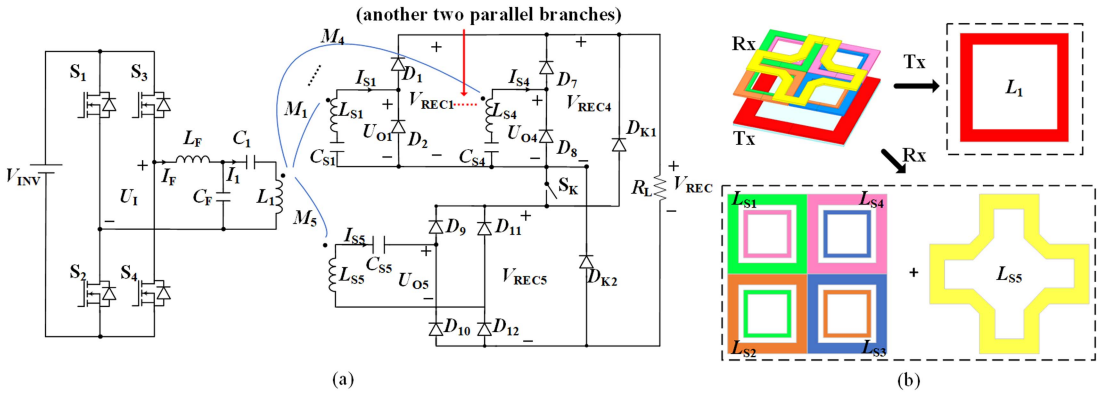

Fig. 2. (a) Proposed series-parallel toggle topology. (b) Coil structures corresponding to topological coils L_1 and L_{S1}–L_{S5}.

to balance the mutual inductance difference caused by different coil sizes. The large cross-shaped coil is connected to the full-bridge rectifier, whereas the four small coils are connected to the half-bridge rectifier such that the output voltage can remain stable. Moreover, the use of four half-bridge rectifiers can reduce the number of diodes.

B. Mathematical Modeling

The angular frequency of the system is ω_1. The resonant conditions of the WPT system can be expressed as

$$\begin{aligned}&\omega_1 L_{\mathrm{F}} - \frac{1}{\omega_1 C_{\mathrm{F}}} = \omega_1 L_1 - \frac{1}{\omega_1 C_1} - \frac{1}{\omega_1 C_{\mathrm{F}}} \\ &= \omega_1 L_{\mathrm{S1}} - \frac{1}{\omega_1 C_{\mathrm{S1}}} = \omega_1 L_{\mathrm{S2}} - \frac{1}{\omega_1 C_{\mathrm{S2}}} = \omega_1 L_{\mathrm{S3}} - \frac{1}{\omega_1 C_{\mathrm{S3}}} \\ &= \omega_1 L_{\mathrm{S4}} - \frac{1}{\omega_1 C_{\mathrm{S4}}} = \omega_1 L_{\mathrm{S5}} - \frac{1}{\omega_1 C_{\mathrm{S5}}} = 0. \end{aligned} \tag{1}$$

Using fundamental harmonic approximation, the relationship between the ac and dc quantities can be deduced as

$$U_I = \frac{2\sqrt{2}}{\pi} V_{\mathrm{INV}}, U_{\mathrm{O}m} = \frac{\sqrt{2}}{\pi} V_{\mathrm{REC}m}, \text{ and } U_{\mathrm{O5}} = \frac{2\sqrt{2}}{\pi} V_{\mathrm{REC5}} \tag{2}$$

where m is 1, 2, 3, or 4.

The different working modes and the corresponding dominant coils in different Rx misalignment regions are shown in Fig. 3. The distance on the axis indicates where the center of Rx is located, that is, the misalignment distance at which the receiver coil is offset. The three different colored zones indicate the three different modes of operation when the Rx center is in that zone. The combination of coils in each boxed region indicates the dominant Tx coils at that location.

This equivalent receiving circuit is shown in Fig. 4. The red and green boxed regions are the equivalent circuits of each of the two layers of Rx coils, respectively. In Fig. 4, M_{xy} ($x = 1, 2,$ or 3; $y = 2, 3,$ or 4) is the mutual inductance between $L_{\mathrm{S}x}$ and $L_{\mathrm{S}y}$. The mathematical model of the coil changes accordingly for the misalignment position. The following three parts analyze the different modes.

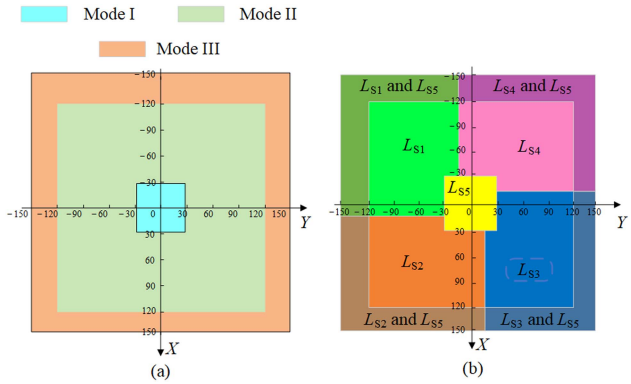

Fig. 3. (a) Different working modes and (b) dominant coils in different Rx misalignment regions.

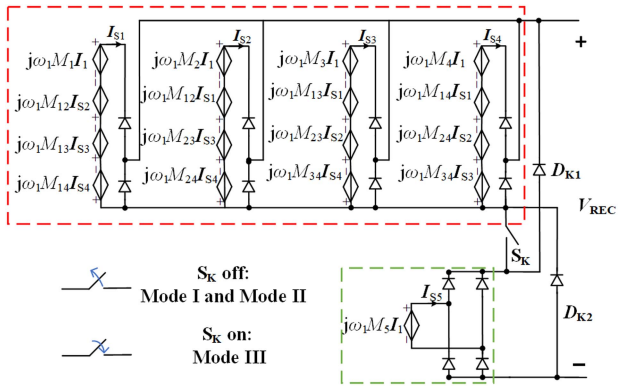

Fig. 4. Equivalent circuit at the receiving side.

1) Mode I: In this mode, $\mathrm{S_K}$ is OFF, and $\mathrm{D_{K1}}$ and $\mathrm{D_{K2}}$ are ON. This mode will take effect when the Rx coils align well with the Tx coils. At this time, the five branches are connected in parallel. The coupling between L_{S5} and Tx is optimal, which results in the largest output voltage of all these five coils. When multiple current-controlled voltage sources are connected in parallel, only the branch with the largest output voltage is connected, and the other branches are disconnected. The output from the

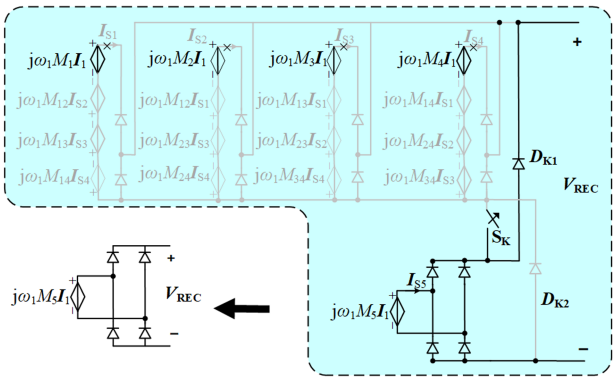

Fig. 5. Mode I: Equivalent circuit of receiving side when L_{S5} dominates.

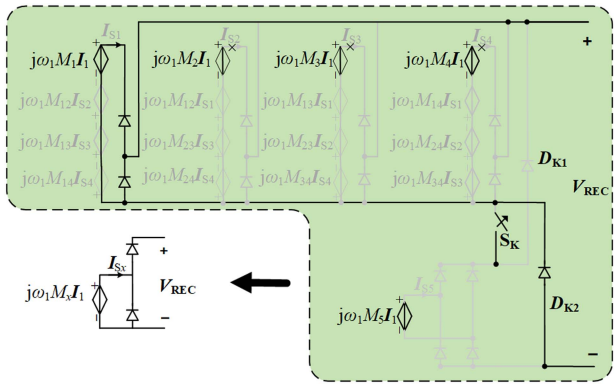

Fig. 6. Mode II: Equivalent circuit at receiving side when L_{Sx} dominates.

cross-coupling of the four small coils can be negligible. The equivalent circuit of Mode I at the Rx side is presented in Fig. 5.

The output voltage, the output current, the output power, and the ac–ac efficiency can be expressed as

$$V_{\mathrm{REC}} = \omega^2 C_{\mathrm{F}} M_5 V_{\mathrm{INV}} \tag{3}$$

$$I_{\mathrm{REC}} = \frac{\omega^2 C_{\mathrm{F}} M_5 V_{\mathrm{INV}}}{R_{\mathrm{L}}} \tag{4}$$

$$P_{\mathrm{OUT}} = \frac{\omega^4 C_{\mathrm{F}}^2 M_5^2 V_{\mathrm{INV}}^2}{R_{\mathrm{L}}} \tag{5}$$

$$\eta = \frac{P_{\mathrm{OUT}}}{P_{\mathrm{OUT}} + I_{\mathrm{F}}^2 R_{\mathrm{LF}} + I_1^2 R_{\mathrm{L1}} + I_{\mathrm{S5}}^2 R_{\mathrm{LS5}}} \tag{6}$$

where R_{LF}, R_{L1}, and R_{LS5} are the equivalent series resistances (ESRs) of the corresponding inductances L_{F}, L_1, and L_{S5}.

2) Mode II: In the second mode, $\mathrm{S_K}$ is OFF, and $\mathrm{D_{K1}}$ and $\mathrm{D_{K2}}$ are ON. This mode will take effect when the Rx coil deviates from the Tx coil (30 mm $<$ |X misalignment| $<$ 150 mm and 30 mm $<$ |Y misalignment| $<$ 150 mm). At this time, the circuit is connected in the same way as Mode I and the dominant coil will be one of the four small coils. For example, when the Rx coil moves to the region of the negative axes of X and Y called the fourth quadrant, L_{S1} has the optimal coupling with L_1. I_{S2}, I_{S3}, I_{S4}, and I_{S5} will tend to zero. The same applies to the other three quadrants. The equivalent receiving circuit of Mode II is presented in Fig. 6. In Fig. 6, $x = 1$, 2, 3, or 4.

The output voltage, the output current, the output power, and the ac–ac efficiency can be expressed as

$$V_{\mathrm{REC}} = 2\omega^2 C_{\mathrm{F}} M_x V_{\mathrm{INV}} \tag{7}$$

$$I_{\mathrm{REC}} = \frac{2\omega^2 C_{\mathrm{F}} M_x V_{\mathrm{INV}}}{R_{\mathrm{L}}} \tag{8}$$

$$P_{\mathrm{OUT}} = \frac{4\omega^4 C_{\mathrm{F}}^2 M_x^2 V_{\mathrm{INV}}^2}{R_{\mathrm{L}}} \tag{9}$$

$$\eta = \frac{P_{\mathrm{OUT}}}{P_{\mathrm{OUT}} + I_{\mathrm{f}}^2 R_{\mathrm{LF}} + I_1^2 R_{\mathrm{L1}} + I_{\mathrm{S}x}^2 R_{\mathrm{LS}x}} \tag{10}$$

where $R_{\mathrm{LS}x}$ is the ESR of the inductance $L_{\mathrm{S}x}$.

3) Mode III: When the Rx coil is moved to the orange regions in Fig. 3, that is, the X misalignment is 150 mm or the Y misalignment is 150 mm, the coupling coefficient between the Tx and the four small coils or the cross-shaped coil decreases dramatically. To smooth the variation of the output voltage in the boundary misalignment regions, Mode III takes effect when $\mathrm{S_K}$ is ON and $\mathrm{D_{K1}}$ and $\mathrm{D_{K2}}$ are OFF. Only one output of the four small coils will be connected with the output of L_{S5} in series. Unlike the fully parallel scheme of the five branches, the output voltage of the boundary regions can be effectively compensated when $\mathrm{S_K}$ is ON. The equivalent receiving circuit of Mode III is presented in Fig. 7.

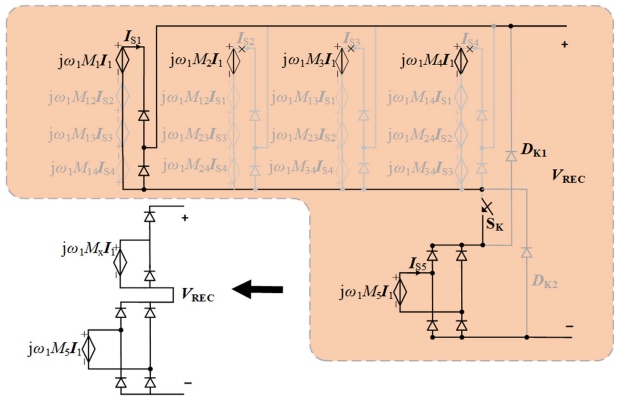

Fig. 7. Mode III: Equivalent circuit at receiving side when dominant coil L_{S1} connected with L_{S5} in series.

The output voltage, the output current, the output power, and the ac–ac efficiency can be expressed as

$$V_{\mathrm{REC}} = \omega^2 C_{\mathrm{F}} V_{\mathrm{INV}} (2M_x + M_5) \tag{11}$$

$$I_{\mathrm{REC}} = \frac{\omega^2 C_{\mathrm{F}} V_{\mathrm{INV}} (2M_x + M_5)}{R_{\mathrm{L}}} \tag{12}$$

$$P_{\mathrm{OUT}} = \frac{\omega^4 C_{\mathrm{F}}^2 V_{\mathrm{INV}}^2 (2M_x + M_5)^2}{R_{\mathrm{L}}} \tag{13}$$

$$\eta = \frac{P_{\mathrm{OUT}}}{P_{\mathrm{OUT}} + I_{\mathrm{F}}^2 R_{\mathrm{LF}} + I_1^2 R_{\mathrm{L1}} + I_{\mathrm{S}x}^2 R_{\mathrm{LS}x} + I_{\mathrm{S5}}^2 R_{\mathrm{LS5}}}. \tag{14}$$

After analyzing three modes under misalignments and comparing the output voltage expressions of three modes, it can be

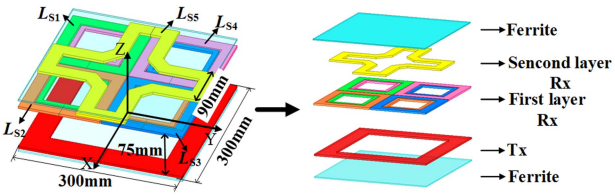

Fig. 8. Layout of magnetic couplers.

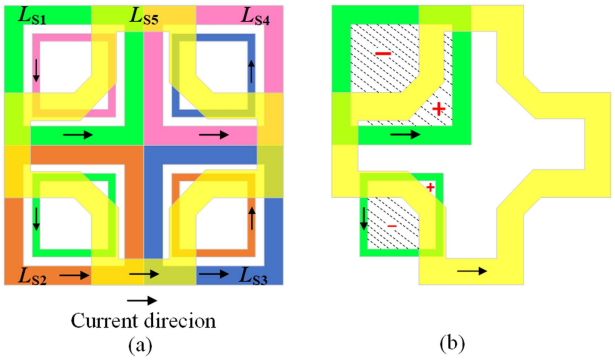

Fig. 9. Structure of receiving coils. (a) Current directions. (b) Decoupling example.

observed that M_5, $2M_x$, and $2M_x+M_5$ are the equivalent effective mutual inductances of three modes, and they are all controllable variables. By adjusting these three equivalent effective mutual inductances to remain smooth in each of the three corresponding regions, a reduction in output fluctuations can be realized. Therefore, the next section describes the process of designing the magnetic coupler to realize the above scheme.

III. Proposed Magnetic Couplers

The structures of magnetic couplers are shown in Fig. 8. The transmitting distance is 75 mm. To ensure that the mutual inductance is large enough during diagonal misalignment, four small coils of the same size are placed in the four corners of the same layer. In the meantime, each coil is connected in series with a small coil, which is nested counterclockwise in adjacent coils, so that when the coils offset along the *X*- and *Y*-axes, the Tx coil and the Rx coils have strong enough coupling to improve the output. Four small coils and their nested coils are combined to form the centrosymmetric Rx coils.

Mutual decoupling between coils is vital to the performance of WPT. In this article, the yellow one is decoupled with the Rx coils of the second layer. The mutual decoupling of the coils simplifies the analysis of the topological mathematical model, and at the same time reduces the interaction between the coils, reduces the current exchange between the coils, reduces the losses, and improves efficiency. Here are generally two decoupling methods, one is to decouple by overlapping coils, and the other is to decouple by nesting decoupled coils. This article takes the first approach. As shown in Fig. 9(a), the current direction of all coils is counterclockwise, so the direction of the magnetic field generated by all coils is facing upward. To take the coil

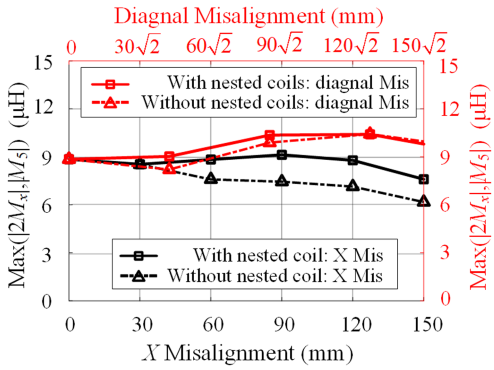

Fig. 10. Max($2|M_x|$, $|M_5|$) with and without nested coils under diagonal and *X* misalignments.

L_{S1} and the cross-shaped coil L_{S5} as a decoupling example, the decoupling principal diagram is portrayed in Fig. 9(b). In the regions where the two coils intersect, the coupling coefficient between L_{S1} and L_{S5} is positive, whereas it is negative in the regions where both do not intersect. After the modification of the sizes of the coils, the sum of these two parts of the coupling coefficient will approach zero, which indicates they are decoupled from each other. So, L_{S1}–L_{S4} are decoupled with L_{S5}.

With nested coils and without nested coils under diagonal and *X* misalignments are shown in Fig. 10. The function Max($2|M_x|$, $|M_5|$) indicates the maximum value of $2|M_x|$ and $|M_5|$. By comparison, it can be learned that magnetic couplers with nested coils can greatly improve the stability of mutual inductance fluctuations in axial misalignments based on ensuring the stability of mutual inductance fluctuations in diagonal misalignments. The equivalent effective mutual inductance increases in the boundary regions with nested coils. The above results and analysis of the simulation are as expected.

To describe the fluctuation of a variable during coil misalignments, we define the volatility as follows:

$$\delta = \frac{X_{\max} - X_{\min}}{X_{\max} + X_{\min}} \times 100\% \tag{15}$$

where δ is the volatility of the variable *X*, and $X_{\max}$ and $X_{\min}$ are the maximum and minimum values of *X*, respectively.

The design flowchart is listed in Fig. 11. N_P is the number of turns of Tx. N_{RX1} is the number of turns of L_{S1}–L_{S4}. $N_{RX1\text{-}2}$ is the number of turns of the nested coils of L_{S1}–L_{S4}. N_{RX2} is the number of turns of L_{S5}.

3-D diagrams of mutual inductance with misalignment of different magnetic couplers are shown in Fig. 12. All these magnetic couplers are unipolar coils (Q), and their Rx coils are unipolar coil (Q), bipolar coil (DD), quadrupolar coil, and the proposed coil, respectively. From this figure, the mutual inductance is high in the middle and low in the periphery when the Rx coil is Q. When the Rx coil is Q or DD, their mutual inductance fluctuations trend seems to be similar. The whole plane is unstable and their absolute values of mutual inductance have zero crossing points. After the above comparison, the advantages of the proposed magnetic couplers are more obvious.

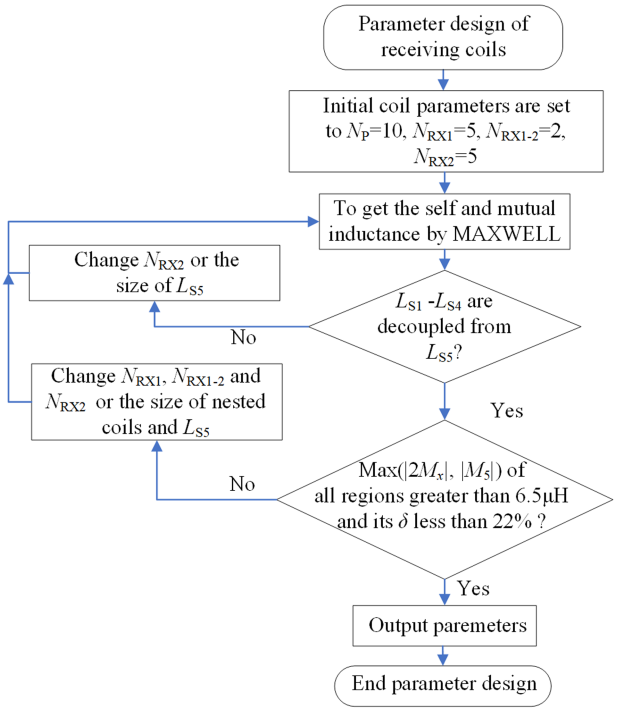

Fig. 11. Design flowchart of magnetic couplers.

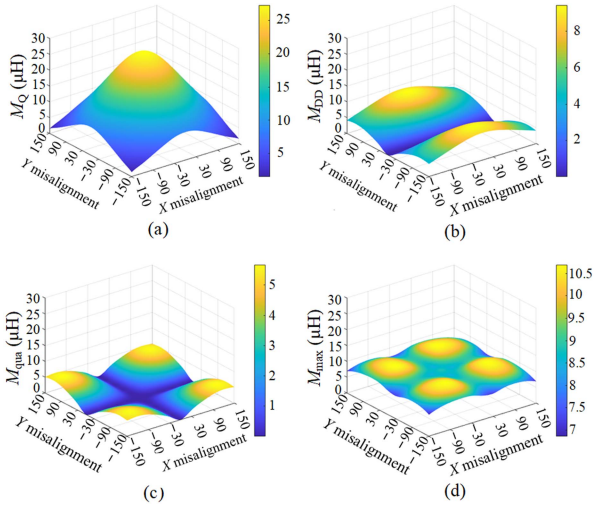

Fig. 12. Simulation of absolute values of mutual inductance for (a) Q to Q, (b) Q to DD, (c) Q to quadrupolar coil, and (d) Max(2$|M_x|$, $|M_5|$) of the proposed magnetic couplers.

This structure not only has a small mutual inductance volatility but also its mutual inductance does not cross zero.

IV. Experimental Validation

To verify the availability of the proposed system, a 926-W prototype is built. The experimental prototype is shown in Fig. 13. S_K, D_{K1}, and D_{K2} are integrated on one printed circuit board (PCB). S_K is a relay. The parameters of the experimental prototype are listed in Table I.

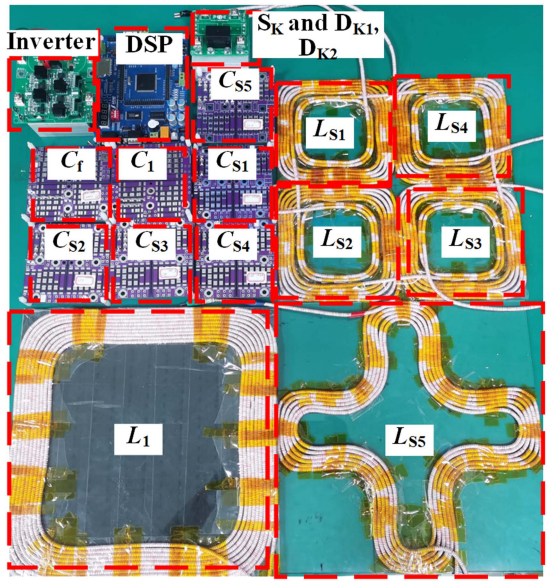

Fig. 13. Photo of the experimental prototype.

TABLE I
Parameters of Experimental Prototype

V_{INV}	200 V	f	85 kHz	R_L	20 Ω
L_F	12.43 μH	L_{S4}	9.58 μH	C_{S2}	371.8 nF
L_1	77.68 μH	L_{S5}	25.45 μH	C_{S3}	364.4 nF
L_{S1}	9.71 μH	C_F	282.1 nF	C_{S4}	366 nF
L_{S2}	9.43 μH	C_1	53.73 nF	C_{S5}	137.8 nF
L_{S3}	9.62 μH	C_{S1}	361.1 nF	N_P	10
N_{RX1}	5	N_{RX1-2}	2	N_{RX2}	6

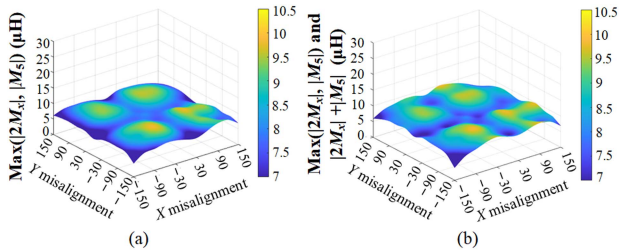

Fig. 14. Experimental results of equivalent mutual inductance of the proposed magnetic couplers. (a) Max(2$|M_x|$, $|M_5|$). (b) Max(2$|M_x|$, $|M_5|$) and 2$|M_x|$+$|M_5|$.

The experimental values of Max(2$|M_x|$, $|M_5|$) and $2|M_x| + |M_5|$ are shown in Fig. 14. The equivalent effective mutual inductances in the boundary regions are smoother than the situation without S_K. Comparing Figs. 12 with 14, the overall mutual inductance values are lower than that of the simulation. The shape of the equivalent effective mutual inductance 3-D diagram of the experimental coils is distorted in some regions, which is caused by errors in the shape and sizes of the experimental wound coils.

The output voltages of mathematical calculation and experimental results when S_K works and does not work are shown in

TABLE II
COMPARISON WITH OTHER METHODS

Comparison	Maximum pad size(mm)	Gap (mm)	Misalignment range (mm) (misalignment percentage)	Load-independent output	Output fluctuation
[17]	450×450	120	Only axial direction *X* misalignment: ±150 mm (33.3%) *Y* misalignment: ±150 mm (33.3%) *Z* misalignment: N/A	No	27.3%
[29]	350×350	80–130	Only axial direction *X* misalignment: ±70 mm (20%) *Y* misalignment: ±70 mm (20%) *Z* misalignment: 50 mm	No	15%
[19]	400×400	150	Only axial direction *X* misalignment: ±150mm (37.5%) *Y* misalignment: ±150mm (37.5%) *Z* misalignment: -2 to +3.5 (23.3%)	CV	5%
[30]	400×400	120	Only axial direction *X* misalignment: ±200 mm (50%) *Y* misalignment: ±50 mm (12.5%) *Z* misalignment: +50 (33.3%)	CC–CV	5%
This article	**300×300**	75	**The whole plane** (|*X* misalignment | < 150 mm and |*Y* misalignment | <150 mm)	**CV**	**21.3%**

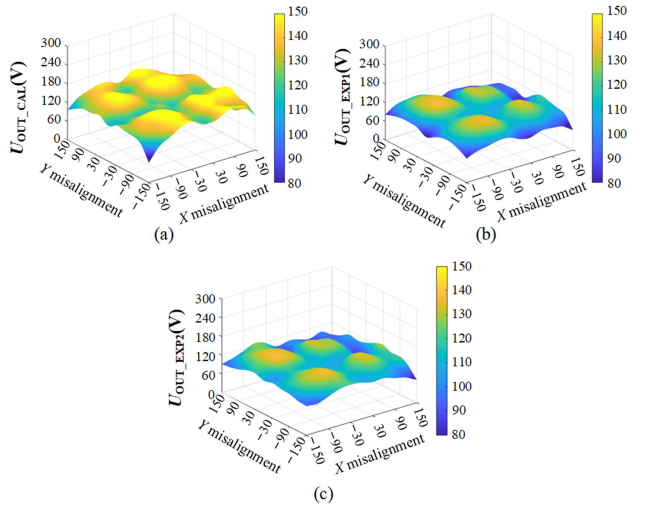

Fig. 15. (a) Output voltage of mathematical calculation when S_K works. (b) Experimental results when S_K does not work. (c) Experimental results when S_K works.

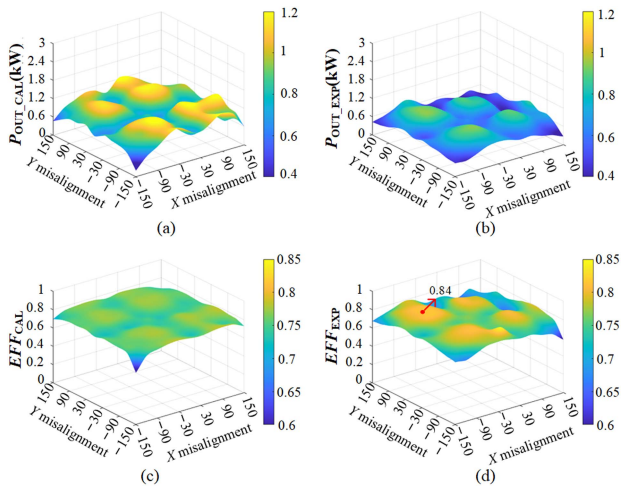

Fig. 16. Output power of (a) calculation and (b) experiment. DC–DC efficiency of (c) calculation and (d) experiment.

Fig. 15. Through the comparison between Fig. 15(a) and (b), it can be seen that when S_K works, the experimental values agree well with the calculated values on the whole, and the experimental values are slightly lower than the calculated values. Apart from the positions where *X* misalignment is 150 mm and *Y* misalignment is 150 mm, δ of Fig. 15(a)–(c) are 17.1%, 26.9%, and 21.3%, respectively, which indicates by introducing Mode III, the output voltage is raised in the boundary regions, and misalignment tolerance performance of the system is improved.

The output power and dc–dc efficiency of the calculation and experiment are shown in Fig. 16. The peak output power of the experiment is 926 W and the average value is 655 W. The trend of calculated output power is almost consistent with that of the experiment. The peak dc–dc efficiency can reach up to 84.5%. The average efficiency is 75.2%. There exist some discrepancies between calculated and experimental results like the asymmetry of the figure and lower output power and efficiency than calculated values. The asymmetry of the figures can be caused by the asymmetry of the hand-wound coils. The actual experimental model has a slight error with the mathematical model.

The experimental waveforms under good alignment are shown in Fig. 17. As can be seen from this figure, the phase of voltage is slightly ahead of the phase of current, which proves that the transmit-side impedance shows weak inductance. Zero voltage switching (ZVS) has been realized, which can actually decrease the loss of switches and stable output.

To show the superiority of the proposed system, the performance of other methods has been compared with the other methods in Table II. Compared with the other four methods,

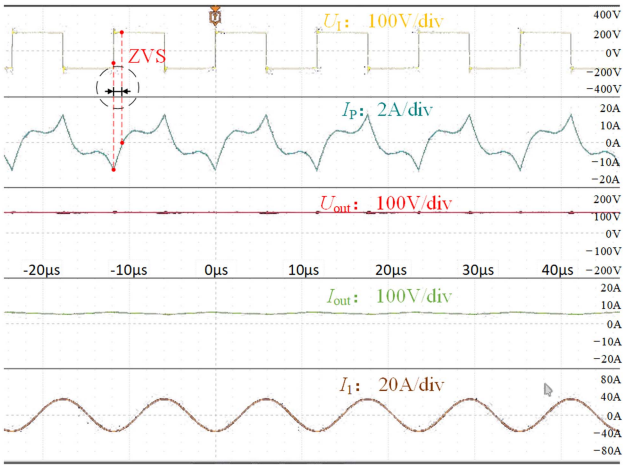

Fig. 17. Experimental waveforms when well aligned.

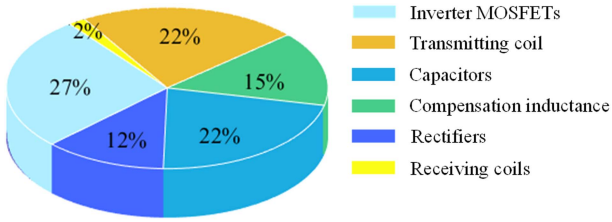

Fig. 18. Loss distribution of the proposed system.

the proposed system has smaller size coils and a wider range of misalignments. Compared with the method presented in [17], the proposed system has a lower output variation. Compared with the methods presented in [17], [27], and [28], the output voltage of this system is load-independent.

The power loss of the IPT system mainly includes the following six parts: the inverter MOSFETs, the transmitting and receiving coils, the compensation capacitors, the compensation inductance, and the rectifiers, as shown in Fig. 18. The losses of the inverter MOSFETs occupy the largest proportion.

V. Conclusion

This article has proposed a WPT system based on reconfigurable adaptive topology and centrosymmetric coils. The adaptive topology can change parallel or series modes by controlling S_K. Centrosymmetric coils contain four unipolar coils that were not decoupled from each other and a cross-shaped coil. The magnetic couplers can keep the equivalent effective mutual inductance stable. The mathematical model of the topology was established and analyzed. Parameters were modified to improve the misalignment tolerance performance of the proposed system. A 655-W experimental prototype was implemented to verify the effectiveness of the proposed IPT system. The volatility of the output voltage was within 21.3%. The misalignment tolerance of the system and ZVS of the inverter has been actually realized.

References

[1] D. Patil, M. K. Mcdonough, J. M. Miller, B. Fahimi, and P. T. Balsara, "Wireless power transfer for vehicular applications: Overview and challenges," *IEEE Trans. Transp. Electrific.*, vol. 4, no. 1, pp. 3–37, Mar. 2018.

[2] R. Xie, R. Liu, X. Chen, X. Mao, X. Li, and Y. Zhang, "An interoperable wireless power transmitter for unipolar and bipolar receiving coils based on three-switch dual-output inverter," *IEEE Trans. Power Electron.*, vol. 39, no. 2, pp. 1985–1989, Feb. 2024, doi: 10.1109/TPEL.2023.3337015.

[3] H. Feng, R. Tavakoli, O. C. Onar, and Z. Pantic, "Advances in high-power wireless charging systems: Overview and design considerations," *IEEE Trans. Transp. Electrific.*, vol. 6, no. 3, pp. 886–919, Sep. 2020.

[4] Y. Wu, H. Wang, Y. Zhuang, and Y. Zhang, "A shared charging channel for power and auxiliary batteries in electric vehicles," *IEEE Trans. Ind. Electron.*, to be published, doi: 10.1109/TIE.2023.3312435.

[5] Y. Zhang et al., "An integrated electric vehicle charging system of wireless power transfer and auxiliary power module with shared converter and magnetic coupler," *IEEE Trans. Ind. Electron.*, to be published, doi: 10.1109/TIE.2023.3331132.

[6] C. Shi, Y. Tang, and A. Khaligh, "A three-phase integrated onboard charger for plug-in electric vehicles," *IEEE Trans. Power Electron.*, vol. 33, no. 6, pp. 4716–4725, Jun. 2018.

[7] Z. Zhang, H. Pang, A. Georgiadis, and C. Cecati, "Wireless power transfer—An overview," *IEEE Trans. Ind. Electron.*, vol. 66, no. 2, pp. 1044–1058, Feb. 2019.

[8] Y. Zhang et al., "Integration of onboard charger and wireless charging system for electric vehicles with shared coupler, compensation, and rectifier," *IEEE Trans. Ind. Electron.*, vol. 70, no. 7, pp. 7511–7514, Jul. 2023.

[9] J. Wu, X. Dai, R. Gao, and J. Jiang, "A coupling mechanism with multidegree freedom for bidirectional multistage WPT system," *IEEE Trans. Power Electron.*, vol. 36, no. 2, pp. 1376–1387, Feb. 2021.

[10] P. Zhao, X. Ji, H. Wang, and M. Fu, "H5-bridge-based bowl-shape wireless charger for multiple loads," *IEEE Trans. Ind. Electron.*, vol. 70, no. 9, pp. 8853–8861, Sep. 2023.

[11] C. Xiao, S. Hao, D. Cheng, and C. Liao, "Safety enhancement by optimizing frequency of implantable cardiac pacemaker wireless charging system," *IEEE Trans. Biomed. Circuits Syst.*, vol. 16, no. 3, pp. 372–383, Jun. 2022.

[12] Z. Yan et al., "Free-rotation wireless power transfer system based on composite anti-misalignment method for AUVs," *IEEE Trans. Power Electron.*, vol. 38, no. 4, pp. 4262–4266, Apr. 2023.

[13] W. Zhou, Q. Gao, R. Mai, Z. He, and A. P. Hu, "Design and analysis of a CPT system with extendable pairs of electric field couplers," *IEEE Trans. Power Electron.*, vol. 37, no. 6, pp. 7443–7455, Jun. 2022.

[14] C. Cai, J. Wang, M. Saeedifard, P. Zhang, R. Chen, and J. Zhang, "Gyrator-gain variable WPT topology for MC-unconstrained CC output customization using simplified capacitance tuning," *IEEE Trans. Ind. Electron.*, vol. 71, no. 4, pp. 3594–3605, Apr. 2024.

[15] V.-B. Vu et al., "Operation of inductive charging systems under misalignment conditions: A review for electric vehicles," *IEEE Trans. Transp. Electrific.*, vol. 9, no. 1, pp. 1857–1887, Mar. 2023.

[16] Y. Zhang et al., "A quadrupole receiving coil with series-connected diode rectifiers for interoperability of nonpolarized and polarized transmitting coils," *IEEE Trans. Power Electron.*, vol. 38, no. 7, pp. 8000–8004, Jul. 2023.

[17] Y. Wu, C. Liu, M. Zhou, X. Mao, and Y. Zhang, "An antioffset electric vehicle wireless charging system based on dual coupled antiparallel coils," *IEEE Trans. Power Electron.*, vol. 38, no. 5, pp. 5634–5637, May 2023.

[18] Y. Chen, R. Mai, Y. Zhang, M. Li, and Z. He, "Improving misalignment tolerance for IPT system using a third-coil," *IEEE Trans. Power Electron.*, vol. 34, no. 4, pp. 3009–3013, Apr. 2019.

[19] Y. Chen et al., "A hybrid inductive power transfer system with misalignment tolerance using quadruple-D quadrature pads," *IEEE Trans. Power Electron.*, vol. 35, no. 6, pp. 6039–6049, Jun. 2020.

[20] A. Hossain, P. Darvish, S. Mekhilef, K. S. Tey, and C. W. Tong, "A new coil structure of dual transmitters and dual receivers with integrated decoupling coils for increasing power transfer and misalignment tolerance of wireless EV charging system," *IEEE Trans. Ind. Electron.*, vol. 69, no. 8, pp. 7869–7878, Aug. 2022.

[21] X. Zhang, X. Ma, Z. Yuan, F. Xu, Z. Chen, and F. Wang, "Misalignment-tolerant integration for S-*LCC*-compensated WPT systems: A complementary-coupling compact receiver," *IEEE Trans. Power Electron.*, vol. 38, no. 10, pp. 11907–11915, Oct. 2023.

[22] Y. Chen, S. He, B. Yang, S. Chen, Z. He, and R. Mai, "Reconfigurable rectifier-based detuned series-series compensated IPT system for anti-misalignment and efficiency improvement," *IEEE Trans. Power Electron.*, vol. 38, no. 2, pp. 2720–2729, Feb. 2023.
[23] Y. Chen et al., "A clamp circuit-based inductive power transfer system with reconfigurable rectifier tolerating extensive coupling variations," *IEEE Trans. Power Electron.*, vol. 39, no. 2, pp. 1942–1946, Feb. 2024, doi: 10.1109/TPEL.2022.3204592.
[24] Y. Zhang et al., "Misalignment-tolerant dual-transmitter electric vehicle wireless charging system with reconfigurable topologies," *IEEE Trans. Power Electron.*, vol. 37, no. 8, pp. 8816–8819, Aug. 2022.
[25] G. Ke, Q. Chen, W. Gao, S.-C. Wong, C. K. Tse, and Z. Zhang, "Research on IPT resonant converters with high misalignment tolerance using multicoil receiver set," *IEEE Trans. Power Electron.*, vol. 35, no. 4, pp. 3697–3712, Apr. 2020.
[26] Z. Li, H. Liu, Y. Huo, J. He, Y. Tian, and J. Liu, "High-misalignment tolerance wireless charging system for constant power output using dual transmission channels with magnetic flux controlled inductors," *IEEE Trans. Power Electron.*, vol. 37, no. 11, pp. 13930–13945, Nov. 2022.
[27] G. Li and H. Ma, "A hybrid IPT system with high-misalignment tolerance and inherent CC–CV output characteristics for EVs charging applications," *IEEE J. Emerg. Sel. Topics Power Electron.*, vol. 10, no. 3, pp. 3152–3160, Jun. 2022.
[28] G. Li, Z. Yao, S. Luo, and H. Ma, "A hybrid IPT system implementing misalignment tolerance and constant current output with primary intermediate coil," *IEEE J. Emerg. Sel. Topics Power Electron.*, vol. 10, no. 6, pp. 7797–7807, Dec. 2022.
[29] G. Ke, Q. Chen, S. Zhang, X. Xu, and L. Xu, "A single-ended hybrid resonant converter with high misalignment tolerance," *IEEE Trans. Power Electron.*, vol. 37, no. 10, pp. 12841–12852, Oct. 2022.
[30] Y. Chen, B. Yang, Z. Kou, Z. He, G. Cao, and R. Mai, "Hybrid and reconfigurable IPT systems with high-misalignment tolerance for constant-current and constant-voltage battery charging," *IEEE Trans. Power Electron.*, vol. 33, no. 10, pp. 8259–8269, Oct. 2018.

Zhongjin Huang was born in Fujian, China. He is currently working toward the M.S. degree in electrical engineering with the School of Electrical Engineering and Automation, Fuzhou University, Fuzhou, China.

His current research focuses on wireless power transfer.

Chao Liu was born in Shanxi, China, in 1997. He is currently working toward the Ph.D. degree in power electronics with the School of Electrical Engineering and Automation, Fuzhou University, Fuzhou, China.

His research interests include power electronics converters and wireless power transfer.

Wenxuan Pan was born in Shanxi, China. He is currently working toward the M.S. degree in electrical engineering with the School of Electrical Engineering and Automation, Fuzhou University Fuzhou, China.

His current research focuses on wireless power transfer.

Xiaoying Chen received the Ph.D. degree in control science and engineering from Central South University, Changsha, China, in 2017. He is currently a Lecturer with the College of Electrical Engineering and Automation, Fuzhou University, Fuzhou, China.

His research interests include modeling and control of power electronics converters and high-efficiency power conversion.

Xingkui Mao (Member, IEEE) received the B.E. and Ph.D. degrees in electrical engineering from Fuzhou University, Fuzhou, China, in 2000 and 2006, respectively.

He is currently a Professor with the College of Electrical Engineering and Automation, Fuzhou University. His research interests include design, manufacturing, and control for power electronic systems and components.

Dr. Mao is the recipient of the IEEE prize paper.

Yiming Zhang (Senior Member, IEEE) received the B.S. and Ph.D. degrees in electrical engineering from Tsinghua University, Beijing, China, in 2011 and 2016, respectively.

He was a Postdoctoral Researcher with San Diego State University, San Diego, CA, USA, and a Research Fellow with Nanyang Technological University, Singapore. He is currently a Full Professor with Fuzhou University, Fuzhou, China. He has authored or coauthored 1 book from Springer and more than 100 technical papers in journals and conference proceedings. His research interests include wireless power transfer and resonant converters.

Dr. Zhang was the Publication Chair of the international conference ICWPT2022. He was the recipient of the Outstanding Doctoral Dissertations of Tsinghua University in 2016. He was recognized as an Outstanding Reviewer for the IEEE TRANSACTIONS ON POWER ELECTRONICS in 2019 and 2022 and a Distinguished Reviewer for the IEEE TRANSACTIONS ON INDUSTRIAL ELECTRONICS in 2020.